Experimental Surface Pressure Data Obtained on 65° Delta Wing Across Reynolds Number and Mach Number Ranges

Volume 2—Small-Radius Leading Edge

Julio Chu and James M. Luckring
Langley Research Center • Hampton, Virginia

The use of trademarks or names of manufacturers in this report is for accurate reporting and does not constitute an official endorsement, either expressed or implied, of such products or manufacturers by the National Aeronautics and Space Administration.

Summary

An experimental wind tunnel test of a 65° delta wing model with interchangeable leading edges was conducted in the Langley National Transonic Facility (NTF). The objective was to investigate the effects of Reynolds and Mach numbers on slender-wing leading-edge vortex flow with four values of wing leading-edge bluntness. The data presented in volume 2 of this report are for a small-radius leading edge equivalent to 0.05 percent of the mean aerodynamic chord. The data for the sharp leading edge and the medium- and large-radius leading edges are presented in volumes 1, 3, and 4, respectively, of this report. Experimentally obtained pressure data for the small-radius leading edge are presented without analysis in tabulated and graphical formats across a Reynolds number range of 6×10^6 to 84×10^6 at a Mach number of 0.85 and across a Mach number range of 0.4 to 0.9 at Reynolds numbers of 6×10^6 and 60×10^6. Normal-force and pitching-moment coefficient plots for these Reynolds number and Mach number ranges are also presented.

Introduction

Wing leading-edge vortex flow on slender wings has been a subject of study at aeronautical research laboratories (refs. 1–6) for many years. The wing upper surface pressure loading induced by the leading-edge vortex has been shown to provide a significant vortex-lift increment at moderate to high angles of attack for slender wings. (See ref. 7.) Application of vortical flow benefits has been primarily directed toward military use for which designs have been investigated that enhance transonic maneuverability for tactical supercruisers using vortex lift (refs. 8 and 9) or that suppress the vortex flow for those conditions where it is undesirable. (See ref. 10.) However, commercial application of vortex flow is evident in the ability of the *Concorde* to achieve high lift during takeoff and landing.

The majority of previous leading-edge vortex flow studies have been conducted on sharp leading-edge wings, where the primary separation line may be assumed to be located at the leading edge. This assumption permits inviscid vortex sheet approximations in analytical modeling and should minimize the dependency of the experimental data on Reynolds number. (See refs. 3–6 and 8.) However, vortical flow investigations on blunt leading-edge wings have been less comprehensive. (See refs. 2, 3, and 11.) The flow around blunt leading edges is inherently dominated by viscous effects and presents a significant challenge for empirical, analytical, or computational analysis. The primary separation line location and the vortex strength for a blunt leading edge are known to be dependent on Reynolds number. This

sensitivity to Reynolds number also occurs with flow reattachments and subsequent development of secondary vortices regardless of leading-edge bluntness. (See refs. 10 and 12.)

Accordingly, the National Aeronautics and Space Administration (NASA) Langley Research Center (LaRC) has attempted to augment the existing database (refs. 11 and 13) for the effects of leading-edge bluntness across a broad Reynolds number range and to facilitate the development of suitable scaling techniques in characterizing the complex leading-edge flows. The approach was to investigate the basic nature of the surface pressure on a slender wing with various values of the leading-edge radius. The experiment was conducted on a planar delta wing with a leading-edge sweep of 65° across broad Reynolds number and Mach number ranges at the Langley National Transonic Facility (NTF). The model was fabricated with removable leading edges to permit testing of four leading-edge sets. The sets were designated as sharp, small, medium, and large, which corresponded to values of leading-edge radii normalized by the mean aerodynamic chord of 0, 0.05, 0.15, and 0.30 percent, respectively.

The experimental data for the small-radius leading edge are presented in volume 2 of this report. The data for the sharp leading edge and for the medium- and large-radius leading edges are presented in volumes 1, 3, and 4, respectively, of this report. Wing pressure data are presented along with normal-force and pitching-moment coefficient data. Note that the primary objective of the force measurements was to monitor the safety of the model support system during the experiment; hence, the accuracy of the force measurements was of secondary importance.

Symbols

a, b, c, d	coefficients in first-blending function φ (appendix A)
b	wing span, 24 in.
C_m	pitching-moment coefficient about moment reference point, $\dfrac{\text{Pitching moment}}{q_\infty S \bar{c}}$
C_N	normal-force coefficient, $\dfrac{\text{Normal force}}{q_\infty S}$
C_p	pressure coefficient, $\dfrac{p - p_\infty}{q_\infty}$
c_R	root chord, 25.734 in.
$\bar{c}$	mean aerodynamic chord, 17.156 in.

F_N	normal force, lbf
l, m, n	coefficients in second-blending function ψ (appendix A)
M_Y	pitching moment, in-lbf
M_∞	free-stream Mach number
p	local pressure, psia
p_∞	free-stream static pressure, psia
p_T	free-stream total pressure, psia
q_∞	free-stream dynamic pressure, psf
R	Reynolds number
r	local radius
S	wing area, 2.145 ft^2
t_T	total temperature, °F
U	uncertainty
x	distance from apex, positive downstream, in.
x_0	initial longitudinal coordinate of blending function φ, in. (appendix A)
x_1	endpoint longitudinal coordinate of blending function φ, in. (appendix A)
y	spanwise distance from apex, positive right, in.
z	distance above X-Y plane, positive upward, in.
α	angle of attack, deg
γ	ratio of specific heats
η	$\dfrac{2y}{b_\iota}$
ξ	nondimensional distance parameter
φ	first-blending function (appendix A)
ψ	second-blending function (appendix A)

Abbreviations:

ESP	electronically scanned pressure
l	lower
L.E., le	leading edge
mac	mean aerodynamic chord
NTF	National Transonic Facility
starb'd	starboard
u	upper
ι	local

Facility

The test was conducted in the Langley National Transonic Facility (NTF). The facility is a fan-driven, closed-circuit, cryogenic transonic pressure wind tunnel.

(See fig. 1.) The test section is 8.2 ft high by 8.2 ft wide by 25 ft long with a slotted ceiling and floor.

The NTF operating capability has a nominal Mach number range of 0.2 to 1.2, total pressure range of 15 to 120 psia, and total temperature range of −260°F to 150°F. The test gas may be dry air or nitrogen. A maximum unit Reynolds of 146×10^6 ft^{-1} is achieved at a Mach number of 1.0. Independent control of pressure, temperature, fan speed, and inlet guide vane angle permits Mach number, Reynolds number, and dynamic pressure to be varied independently within the wind tunnel operational envelope.

To reduce turbulence, four antiturbulence screens were installed in the settling chamber, and a 15:1 contraction from settling chamber to nozzle throat was provided. To minimize wall interference, the test section floor and ceiling were set at 0°, model support walls at −1.76°, and reentry flaps at 0°. Acoustic treatment upstream and downstream of the fan was incorporated to reduce fan noise. More details of the wind tunnel physical characteristics and operations can be found in reference 14.

Model Description and Test Apparatus

The basic layout of the delta wing model is shown in figure 2(a). The wing has a leading-edge sweep of 65°, no twist or camber, and four sets of interchangeable leading edges, which attach to the flat plate part of the wing. The four leading-edge streamwise contours are illustrated in figure 2(b). The model root chord is 25.734 in., the wing span is 24 in., and the maximum wing thickness is 0.875 in. The wing was fabricated from VascoMax C-200,[1] which is suitable for cryogenic operation, and had a surface finish specification of 8 microinches. Figure 2(c) is a photograph of three of the leading-edge sets; one set is attached to the flat plate part of the model. With the exception of the seam at the plane of symmetry, where the left and right side leading edges are joined, each interchangeable leading-edge set (which includes part of the outboard trailing edge) was fabricated as one continuous piece of hardware. This eliminated the surface discontinuities typically associated with an upper and lower leading-edge surface parting line.

The wing and sting surfaces are represented by a fully analytical function with continuity through the second derivative and, hence, curvature. However, the wing-sting intersection line exhibits a discontinuity in slope across it. The leading- and trailing-edge cross-sectional shapes are constant spanwise except for a region near the wingtip where the two shapes intersect. A

---

[1]Trademark of Teledyne Vasco.

detailed geometric description of the various regions of the delta wing and sting (fig. 3) is presented in appendix A. Unless otherwise noted, all quantities have been normalized by the wing root chord.

The model was supported (fig. 4(a)) at the aft end by the model sting, 10°-bent sting, and stub sting. The total model support system confined the center of rotation of the model to the center of the test section. The bent sting extended the positive angle-of-attack range up to approximately 30°.

The model had 183 surface static pressure ports with each having an inside diameter of 0.010 in. The orifice size selection was based on prior cryogenic model-testing experience (ref. 15) at the Langley 0.3-Meter Transonic Cryogenic Tunnel (0.3-m TCT). The majority of the ports were located on the upper surface of the right side (i.e., starboard side) of the model. They were located at nondimensional longitudinal stations of $x/c_R = 0.20$, 0.40, 0.60, 0.80, and 0.95. (See fig. 2(a).) At each chord station, the orifices were situated at constant fractions of local semispan so that they were aligned along rays emanating from the wing apex. The upper surface orifices were located every 5 percent of the local semispan out to one half of the local semispan, beyond which, they were spaced every 2.5 percent of the local semispan. The lower surface pressure ports were located on the left side (i.e., port side) of the model at the same longitudinal stations as on the starboard side. At each chord station, the lower surface orifices were located at local semispan stations of 0.20, 0.40, 0.60, 0.70, 0.80, 0.85, 0.90, and 0.95. In addition, orifices were located directly on both the port and starboard leading edges (except for the sharp leading-edge set) at every 10-percent root chord as well as at the 0.95-chord station. Pressure port location dimensions are shown in tables 1, 2, and 3. Locations that did not have pressure ports are indicated by dashed-line entries.

Instrumentation

Surface static pressure measurements were obtained with four 48-port, 30-psid electronically scanned pressure (ESP) modules. Because of limited volume within the model and its immediate vicinity, the ESP modules were secured inside the enclosure of the wind tunnel pitch system downstream of the stub sting. These modules were placed in a heated container to ensure operation in a cryogenic environment. All model pressure tubes were routed downstream through the sting system and connected to the ESP modules.

Cryogenically rated strain gages configured for two moment bridges were installed on the model sting. These gages were used to monitor model support system safety during the test. One bridge was located at the wing

trailing-edge longitudinal station and the second 4 in. downstream of the wing trailing edge. In figure 4(b), note gage locations at the two rings around the sting just aft of the wing trailing edge. These gages were configured to Poisson ratio full bridges and were shielded from the free stream by a protective chemical coating. Normal force and pitching moment were calculated from measurements of these gages and reported as nondimensional coefficients.

Model angle of attack was determined from the wind tunnel arc-sector angles measured during the test and from sting bending characteristics that were obtained during pretest loadings. The sting fairing cavity volume was insufficient for installation of a fully heated onboard accelerometer package to measure inertial model angles during cryogenic operations.

Measurement Accuracy

The Beattie-Bridgman gas model (ref. 16) and the quoted specifications for the instrumentation were applied to approximate the accuracies of the test parameters and the aerodynamic coefficients. The technique of Kline and McClintock, as specified by Holman (ref. 17), was used to calculate the coefficient accuracies. The uncertainties U of the measurements of the normal-force coefficient C_N, pitching-moment coefficient C_m, pressure coefficient C_p, and free-stream Mach number M_∞ depend on the uncertainties of their respective primary measurements. Estimates of measurement accuracies are presented in appendix B.

The quoted accuracy of an ESP module is ±0.1 percent of the instrument maximum pressure. Therefore, the accuracy of the 30-psid ESP modules used in this test is ±0.03 psid.

Data Reduction and Corrections

Data reduction methods used for the pressure data and wind tunnel parameters were those outlined in reference 16. To obtain force and moment data, the strain gages on the sting were treated as two-component strain gage balances in the data reduction procedure. (See ref. 18.) Because the Reynolds number range was achieved at only two test temperatures for the various total pressures, aeroelastic effects (i.e., model deformation due to pressure) can distort the true Reynolds number effects. However, the aeroelastic effect on the aerodynamic data is small because of the relatively high stiffness resulting from the model thickness and low-aspect-ratio planform as well as the support system structure as illustrated in figure 4(a). Measurements for an inverted model attitude were not taken, and a nominal

3

flow angularity correction of +0.13° (upflow) was applied to the reported angles of attack.

Test Program

Figure 5 shows the combinations of Reynolds numbers and free-stream Mach numbers used for the test. The test matrix shows that a Mach number of 0.85 was selected for the study of the Reynolds number effects and that Reynolds numbers of 6×10^6 and 60×10^6 were selected for the study of Mach number effects. All data were obtained with free boundary layer transition.

Data Presentation

Pressure data measured on the delta wing are presented for each data point in tabular and graphical formats in appendixes C–E. Normal-force and pitching-moment data for each angle of attack are presented in figures 6–8. The moment reference point was located at two thirds of the root chord aft of the wing apex. The angle of attack ranged nominally from −1° to 27°.

Wing pressure coefficients are tabulated for each data point and accompanied by a surface pressure distribution plot and a leading-edge pressure plot. The degree of similarity between the port and starboard leading-edge pressure plots indicates the extent of flow symmetry. Note that coefficient value represented by a series of asterisks in tables C1–C7, D1–D6, and E1–E6 is either an unrecorded or an apparently erroneous pressure port measurement.

The pressure coefficient data test matrix is presented in table 4. The test breakdown is as follows: data for Reynolds numbers from 6×10^6 to 84×10^6 at $M_\infty = 0.85$ are given in appendix C, data for a Reynolds number of 6×10^6 at $M_\infty = 0.40$ to 0.90 are given in appendix D, and data for a Reynolds number of 60×10^6 at $M_\infty = 0.40$ to 0.90 are given in appendix E.

Summary Remarks

Pressure data obtained from a 65° delta wing with the small-radius leading edge (i.e., 0.05 percent of mac) are presented in the form of surface pressure plots and leading-edge pressure plots for a Reynolds number range of 6×10^6 to 84×10^6 at a Mach number of 0.85 and a Mach number range of 0.4 to 0.9 at Reynolds numbers of 6×10^6 and 60×10^6. Although upper and lower surface pressures were measured on opposite sides of the model, model symmetry permitted pressure distribution plots to be superimposed on a sketch of the half wing. The plots of the leading-edge pressures indicate the extent of flow symmetry by comparing port and starboard leading-edge pressures. Normal-force and pitching-moment coefficient plots for Reynolds number and Mach number ranges are also presented.

NASA Langley Research Center
Hampton, VA 23681-0001
August 11, 1995

Table 1. Wing Upper Surface Pressure Port Locations on Starboard Side

η	x/c_R of—									
	0.20		0.40		0.60		0.80		0.95	
	x, in.	y, in.	x, in.	y, in.	x, in.	y, in.	x, in.	y, in.	x, in.	y, in.
0.050	5.147	0.120	10.294	0.240	15.440	0.360	------	------	------	------
.100		.240		.480		.720	------	------	------	------
.150		.360		.720		1.080	------	------	------	------
.200		.480		.960		1.440	------	------	24.447	2.280
.250	------	------		1.200		1.800	20.587	2.400		2.850
.300	5.147	0.720		1.440		2.160		2.880		3.420
.350		.840		1.680		2.520		3.360		3.990
.400		.960		1.920		2.880		3.840		4.560
.450		1.080		2.160		3.240		4.320		5.130
.500		1.200		2.400		3.600		4.800		5.700
.525	------	------		2.520		3.780		5.040		5.985
.550	5.147	1.320		2.640		3.960		5.280		6.270
.575	------	------		2.760		4.140		5.520		6.550
.600	5.147	1.440		2.880		4.320		5.760		6.840
.625	------	------	------	------		4.500		6.000		7.125
.650	5.147	1.560	10.294	3.120		4.680		6.240		7.410
.675	------	------		3.240		4.860		6.480		7.695
.700	5.147	1.680		3.360		5.040		6.720		7.980
.725	------	------		3.480		5.220		6.960		8.265
.750	5.147	1.800		3.600	------	------		7.200		8.550
.775	------	------		3.720	15.440	5.580		7.440		8.835
.800	5.147	1.920		3.840		5.760		7.680		9.120
.825	------	------		3.960		5.940		7.920		9.405
.850	5.147	2.040		4.080		6.120		8.160		9.690
.875	------	------		4.200		6.300		8.400		9.975
.900	5.147	2.160		4.320		6.480		8.640		10.260
.925	------	------		4.440		6.660		8.880		10.545
.950	5.147	2.280		4.560		6.840		9.120		10.830
.975	------	------		4.680		7.020		9.360		11.115
1.000	5.147	2.400		4.800		7.200		9.600		11.400

Table 2. Wing Lower Surface Pressure Port Locations on Port Side

| | x/c_R of— | | | | | | | | | |
| | 0.20 | | 0.40 | | 0.60 | | 0.80 | | 0.95 | |
η	x, in.	y, in.	x, in.	y, in.	x, in.	y, in.	x, in.	y, in.	x, in.	y, in.
−0.200	5.147	−0.480	10.294	−0.960	15.440	−1.440	------	------	24.447	−2.280
−.400		−.960		−1.920		−2.880	20.587	−3.840		−4.560
−.600		−1.440		−2.880		−4.320		−5.760		−6.840
−.700		−1.680		−3.360		−5.040		−6.720		−7.980
−.800		−1.920		−3.840		−5.760		−7.680		−9.120
−.850		−2.040		−4.080		−6.120		−8.160		−9.690
−.900		−2.160		−4.320		−6.480		−8.640		−10.260
−.950		−2.280		−4.560		−6.840		−9.120		−10.830
−.975	------	------		−4.680		−7.020		−9.360		−11.115
−1.000	5.147	−2.400		−4.800		−7.200		−9.600		−11.400

Table 3. Wing Leading-Edge Pressure Port Locations on Starboard Side

| | x/c_R of— | | | | | | | | | |
| | 0.10 | | 0.30 | | 0.50 | | 0.70 | | 0.90 | |
η	x, in.	y, in.	x, in.	y, in.	x, in.	y, in.	x, in.	y, in.	x, in.	y, in.
1.000	2.573	1.200	7.720	3.600	12.867	6.000	18.014	8.400	23.161	10.800

Table 4. Pressure Coefficient Data Test Matrix for Small-Radius Leading Edge

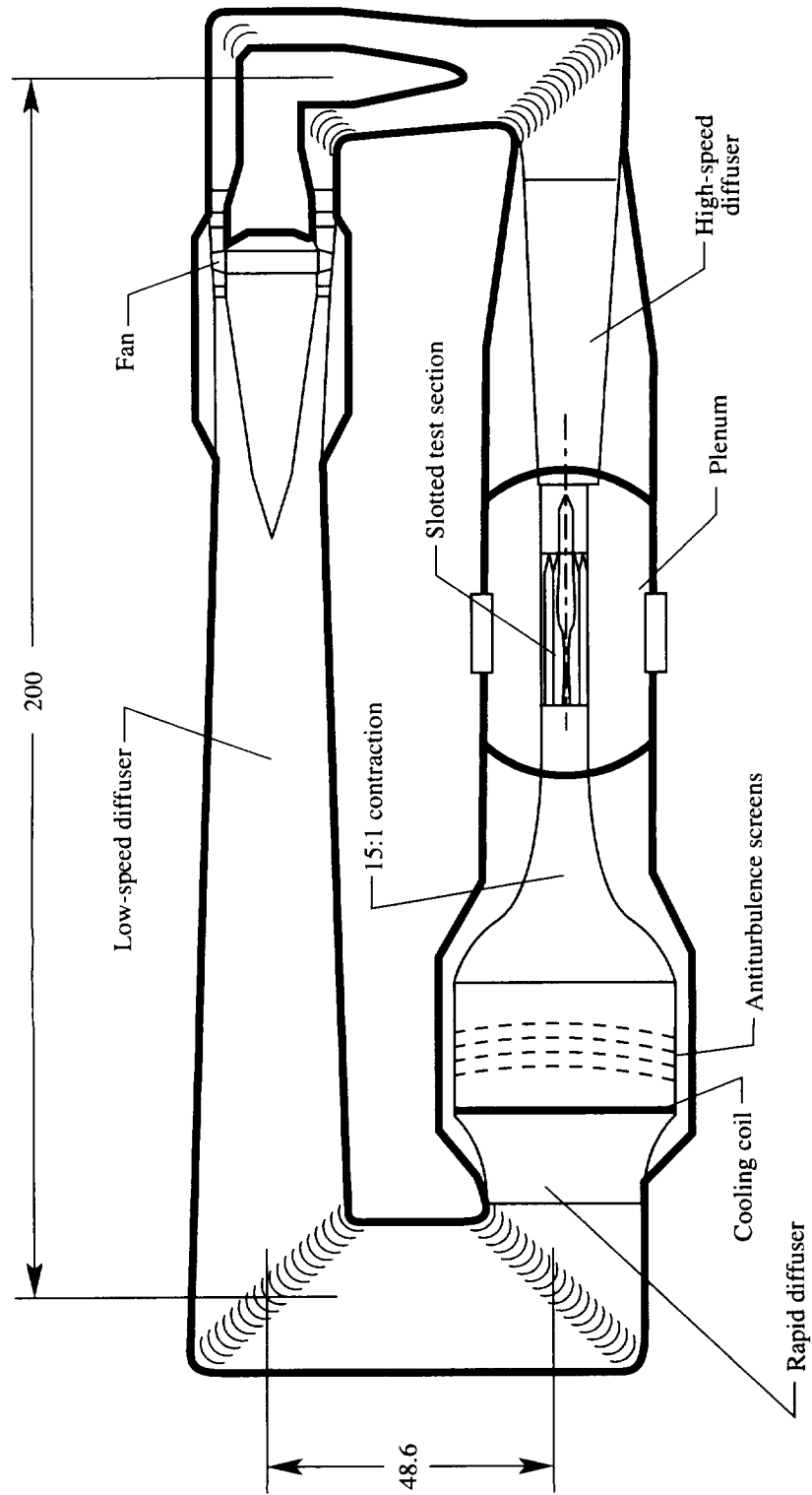| Appendix table	Run	Mach	R_{mac}	q_∞, psf	t_T, °F
C1	41	0.85	6×10^6	722	120
C2	35		12	1444	120
C3	53		24	690	−250
C4	54		36	1035	
C5	52		60	1725	
C6	51		72	2068	
C7	50		84	2413	
D1	36	0.40	6	387	120
D2	38	.60		555	
D3	39	.80		692	
D4	40	.83		710	
D5	42	.87		733	
D6	43	.90		750	
E1	44	.40	60	950	−250
E2	45	.60		1344	
E3	46	.80		1659	
E4	47	.83		1699	
E5	48	.87		1749	
E6	49	.90		1785	

Figure 1. Langley National Transonic Facility circuit. Linear dimensions are in feet.
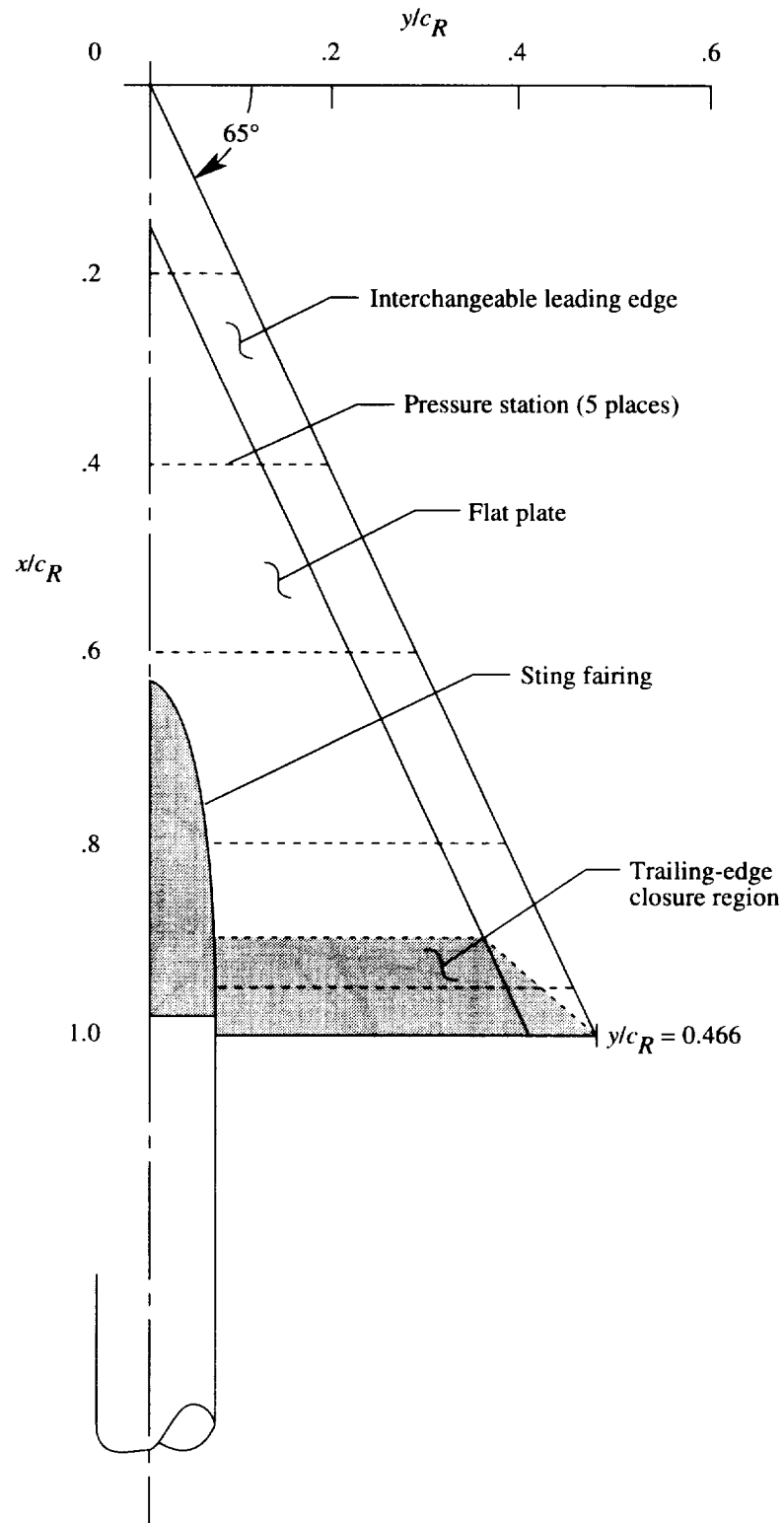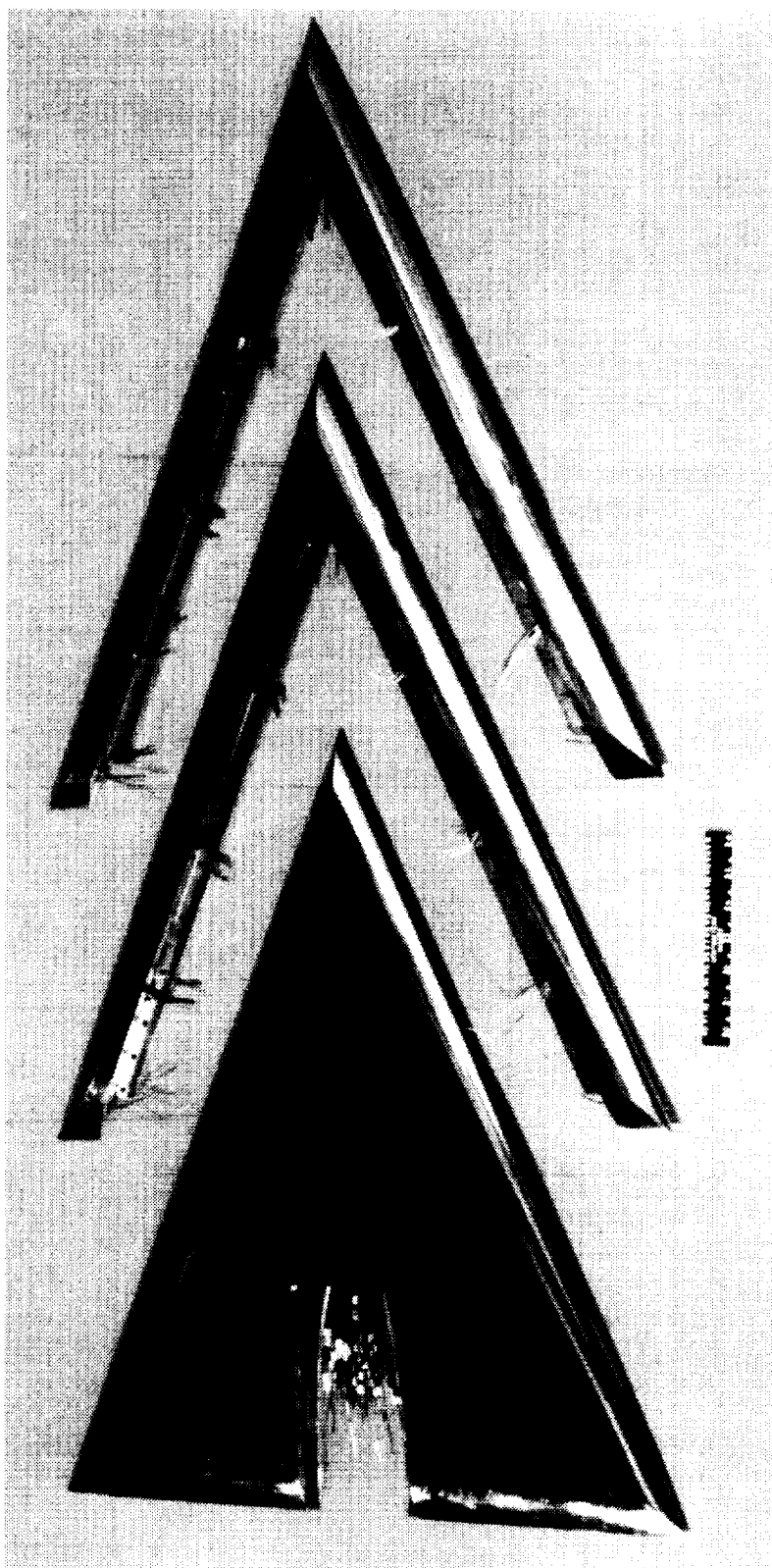
(a) Model configuration.

Figure 2. Delta wing model.
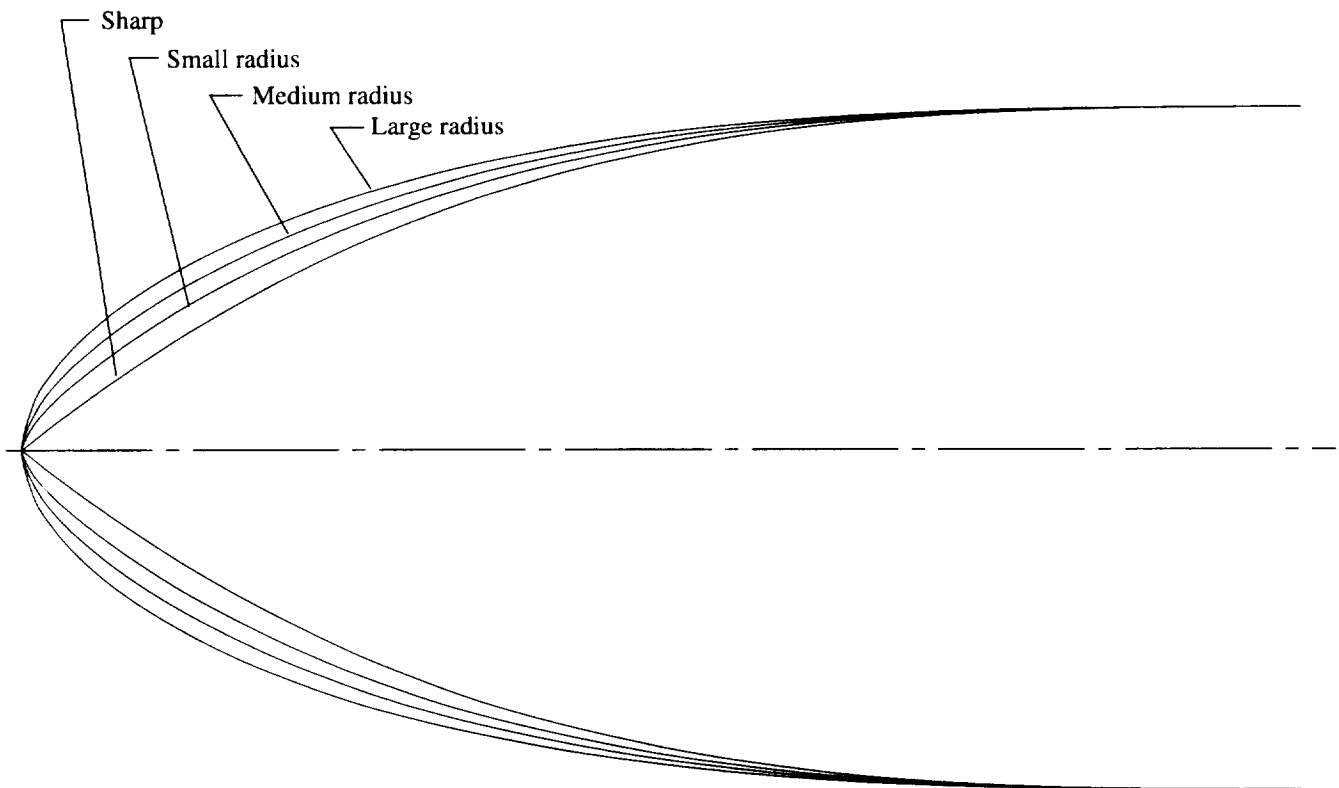
(b) Streamwise leading-edge contours (not to scale).

Figure 2. Continued.

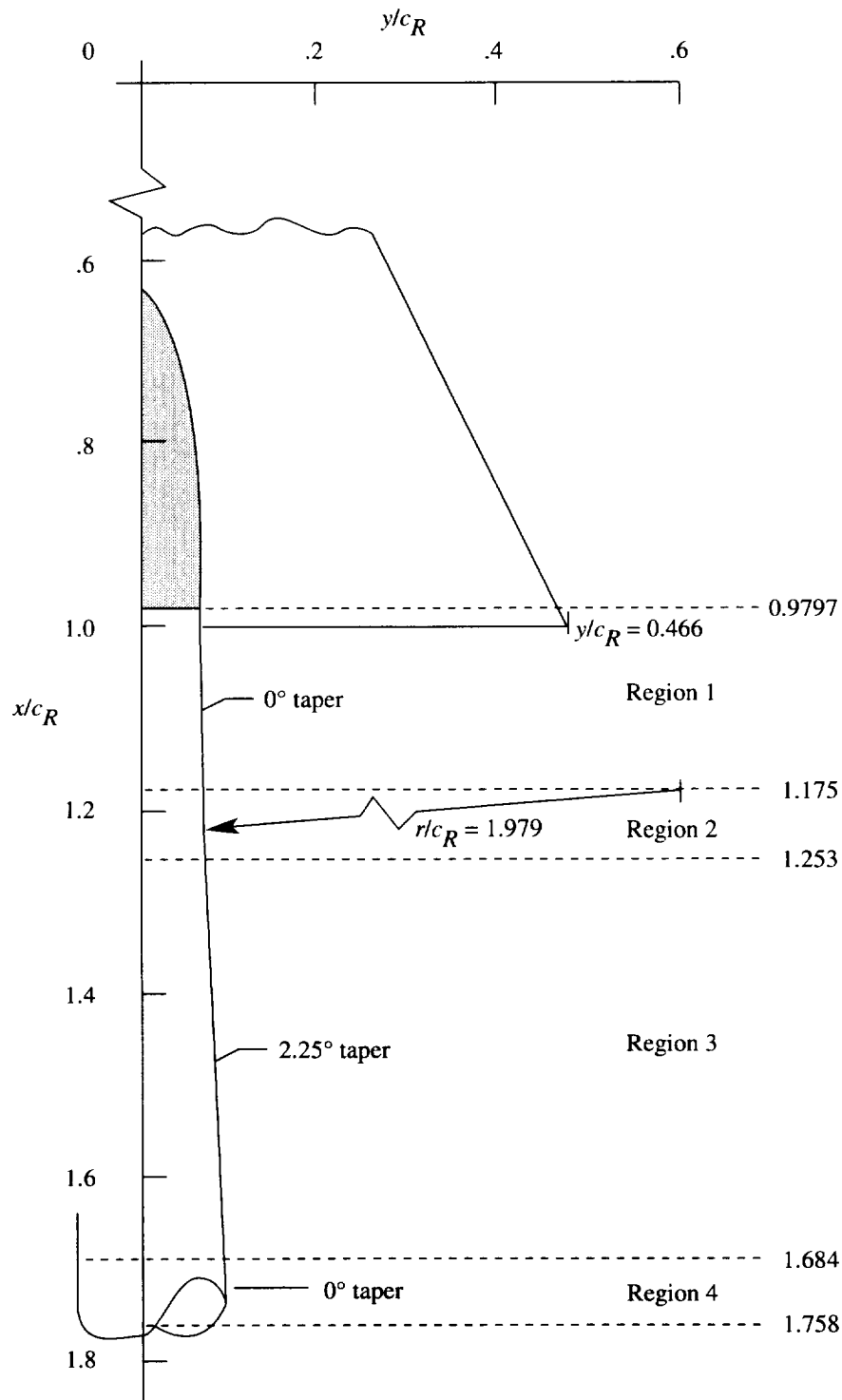(c) Model with three leading-edge sets.

Figure 2. Concluded.

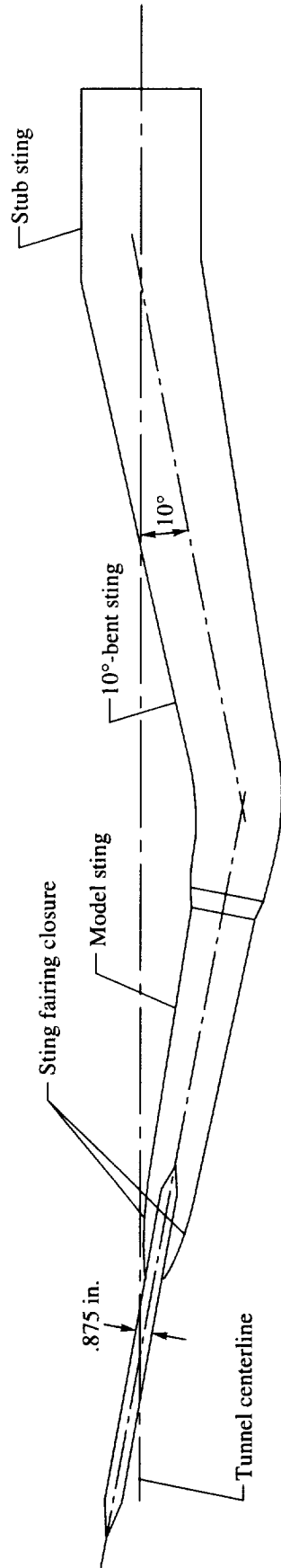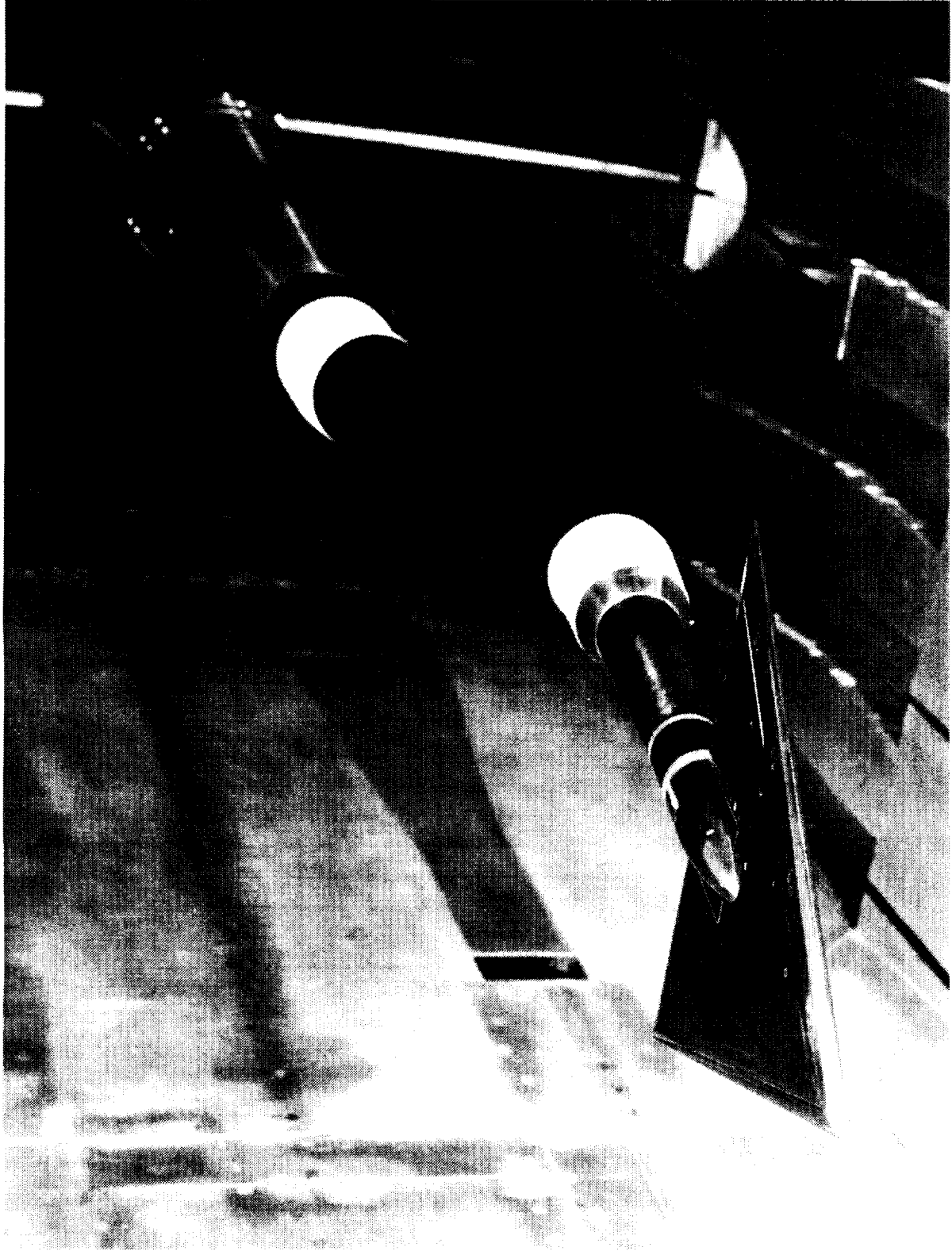Figure 3. Delta wing model fore-sting detail.

Stub sting

10°-bent sting

10°

Model sting

Sting fairing closure

.875 in.

Tunnel centerline

(a) Model and sting system profile.

Figure 4. The 65° delta wing model assembly and support system.

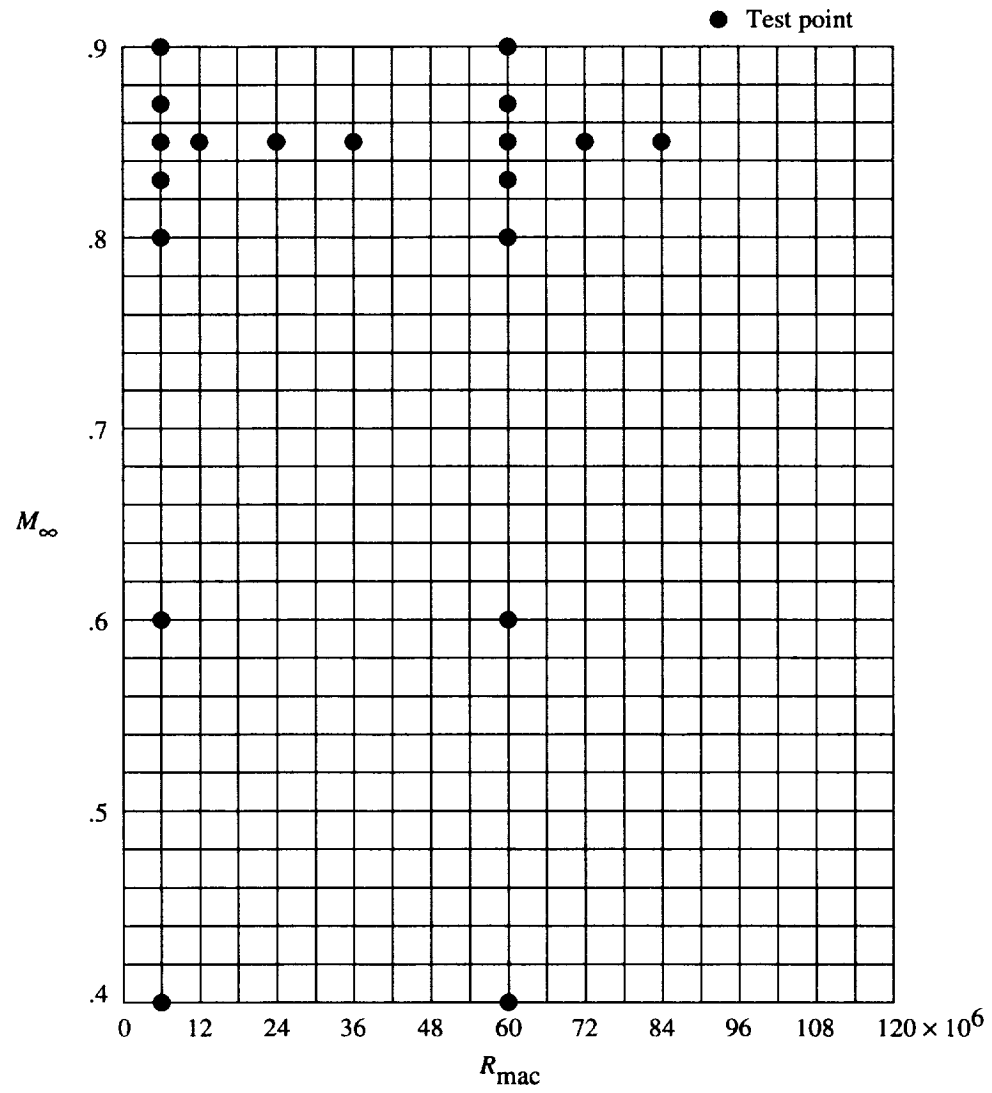(b) Installation in Langley National Transonic Facility.

Figure 4. Concluded.

13

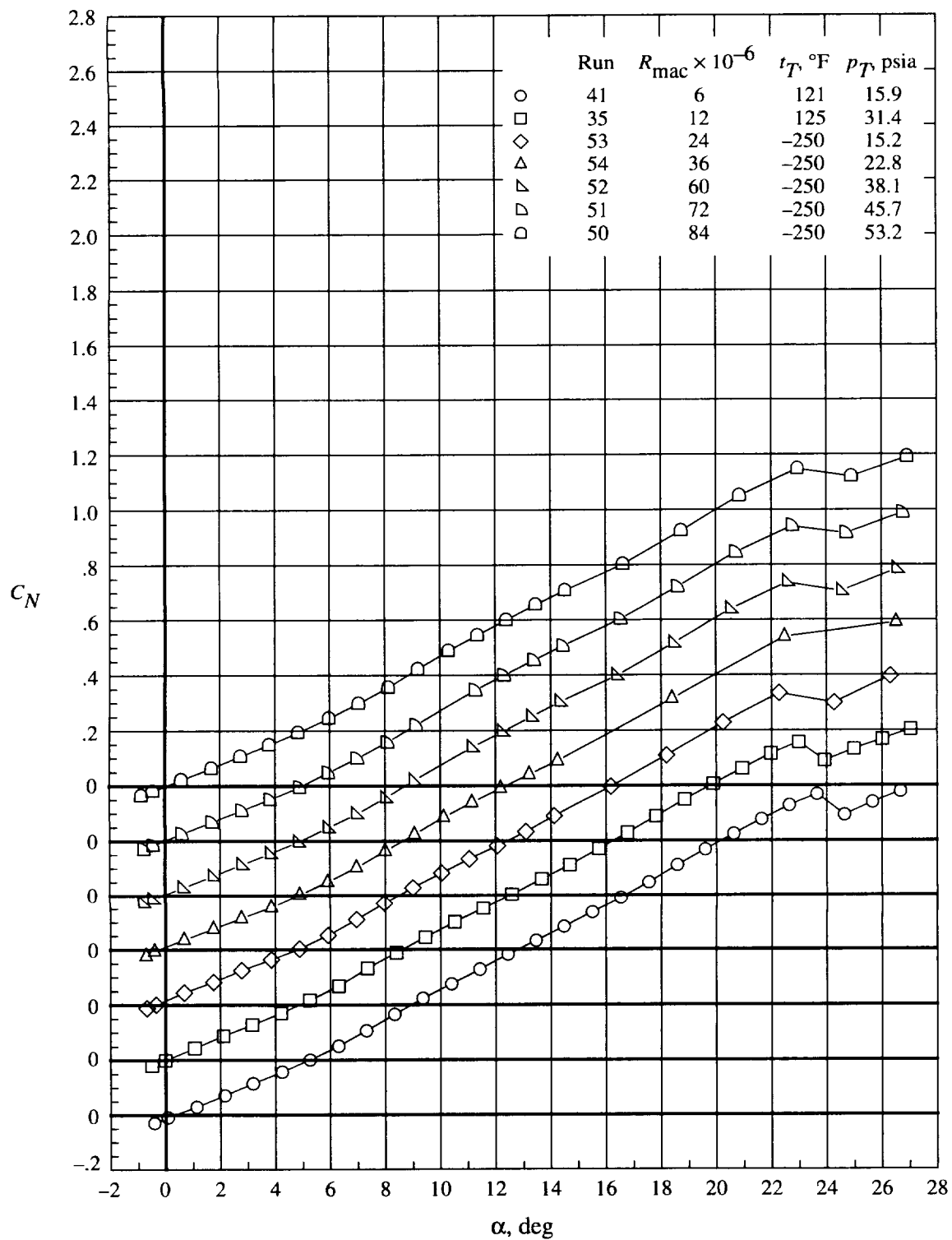Figure 5. Test matrix for 65° delta wing with small-radius leading edge.

(a) C_N versus α.

Figure 6. Normal-force and pitching-moment coefficients at angles of attack for wing with small-radius leading edge. $M_\infty \approx 0.85$.

(b) C_m versus α.

Figure 6. Concluded.

16

(a) C_N versus α.

Figure 7. Normal-force and pitching-moment coefficients at angles of attack for wing with small-radius leading edge. $R_{mac} \approx 6 \times 10^6$.

(b) C_m versus α.

Figure 7. Concluded.

18

(a) C_N versus α.

Figure 8. Normal-force and pitching-moment coefficients at angles of attack for wing with small-radius leading edge. $R_{mac} \approx 60 \times 10^6$.
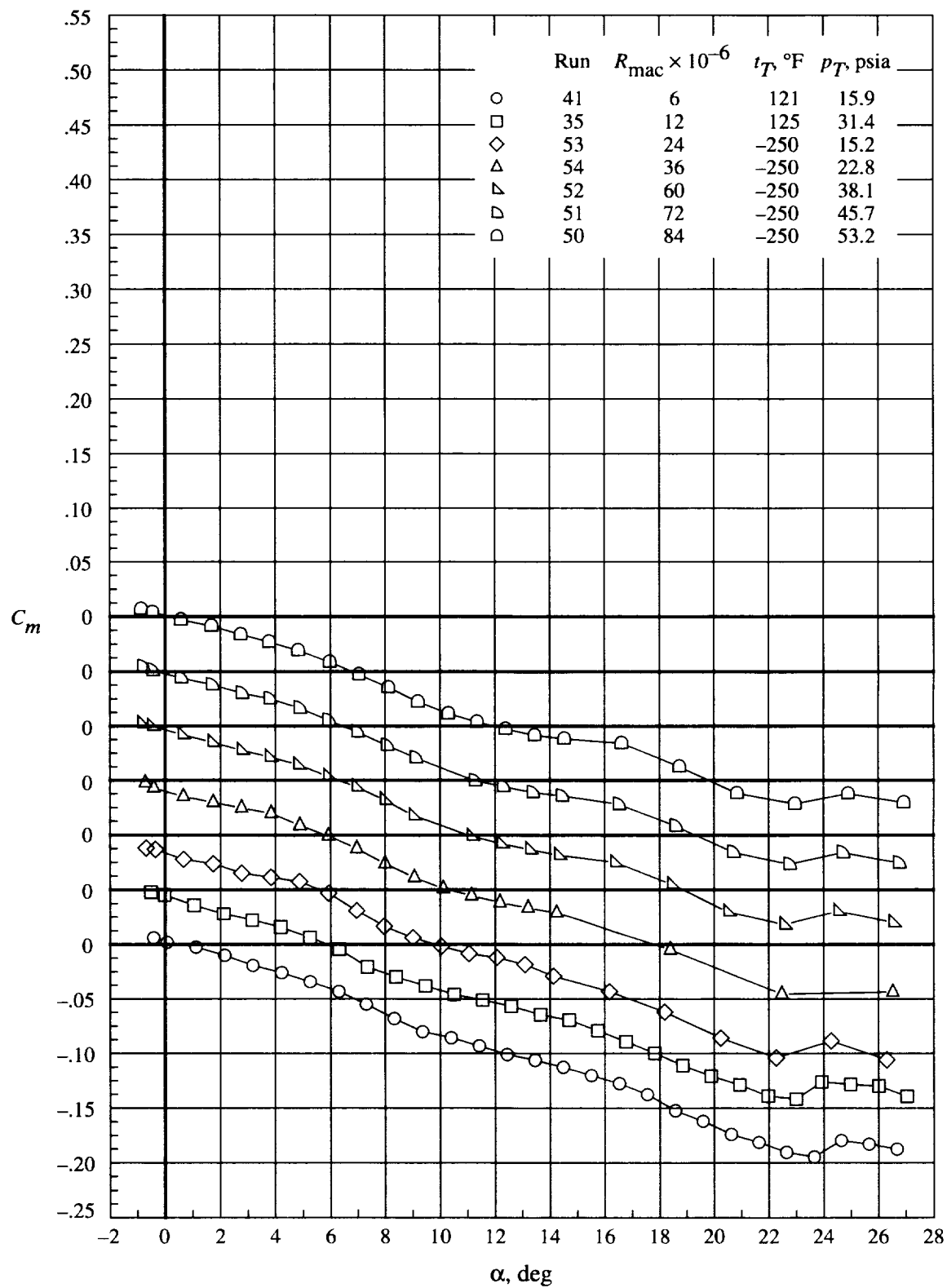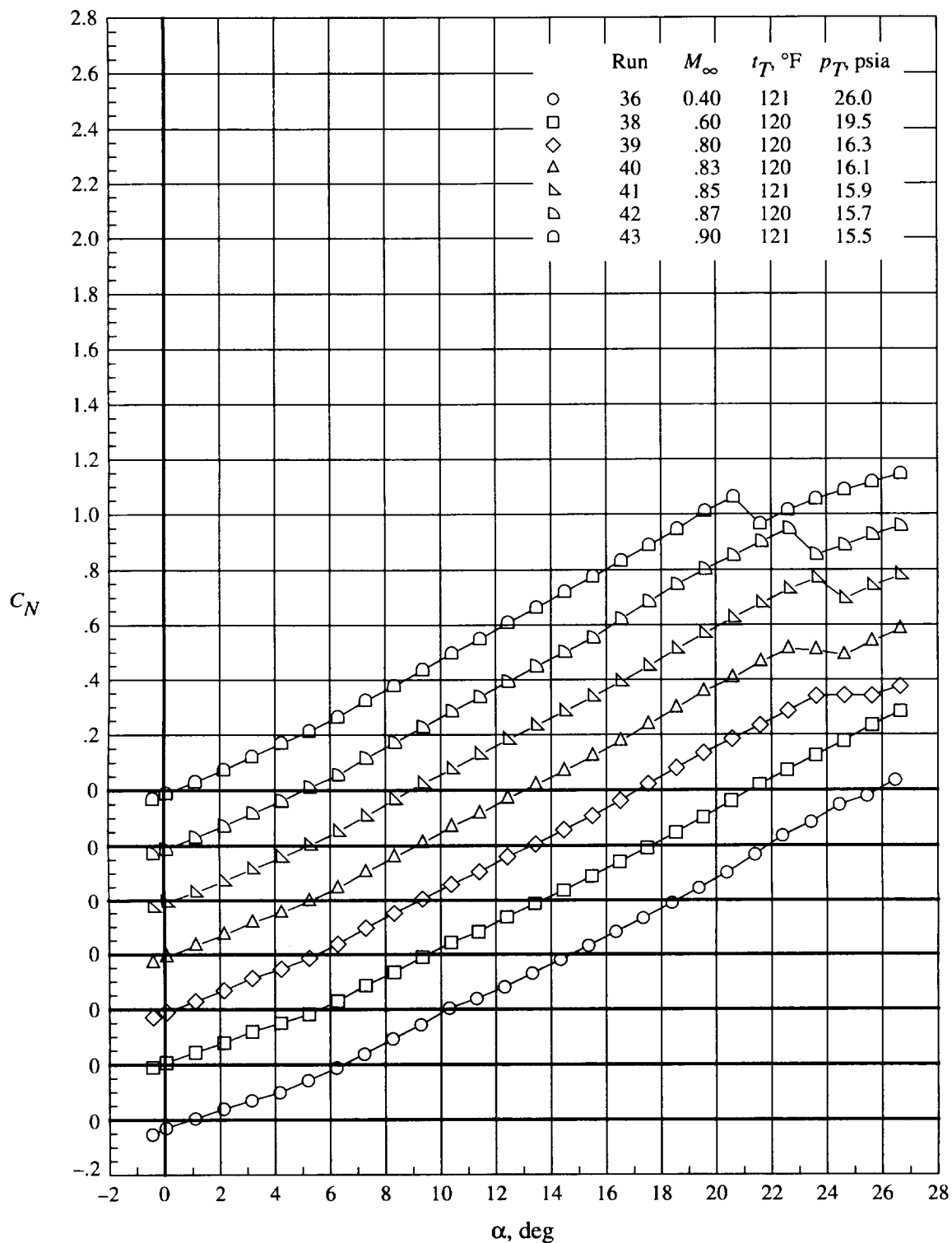
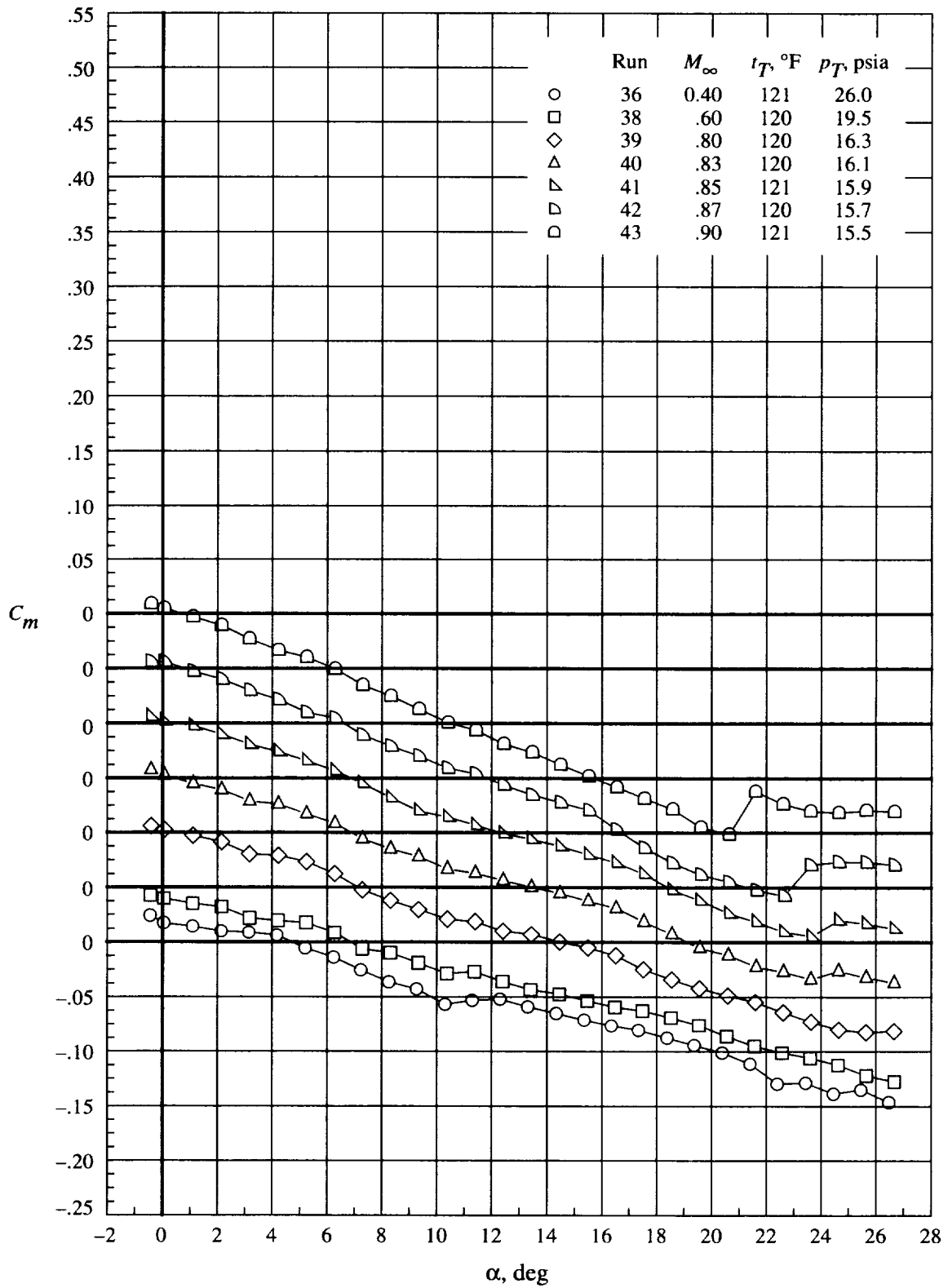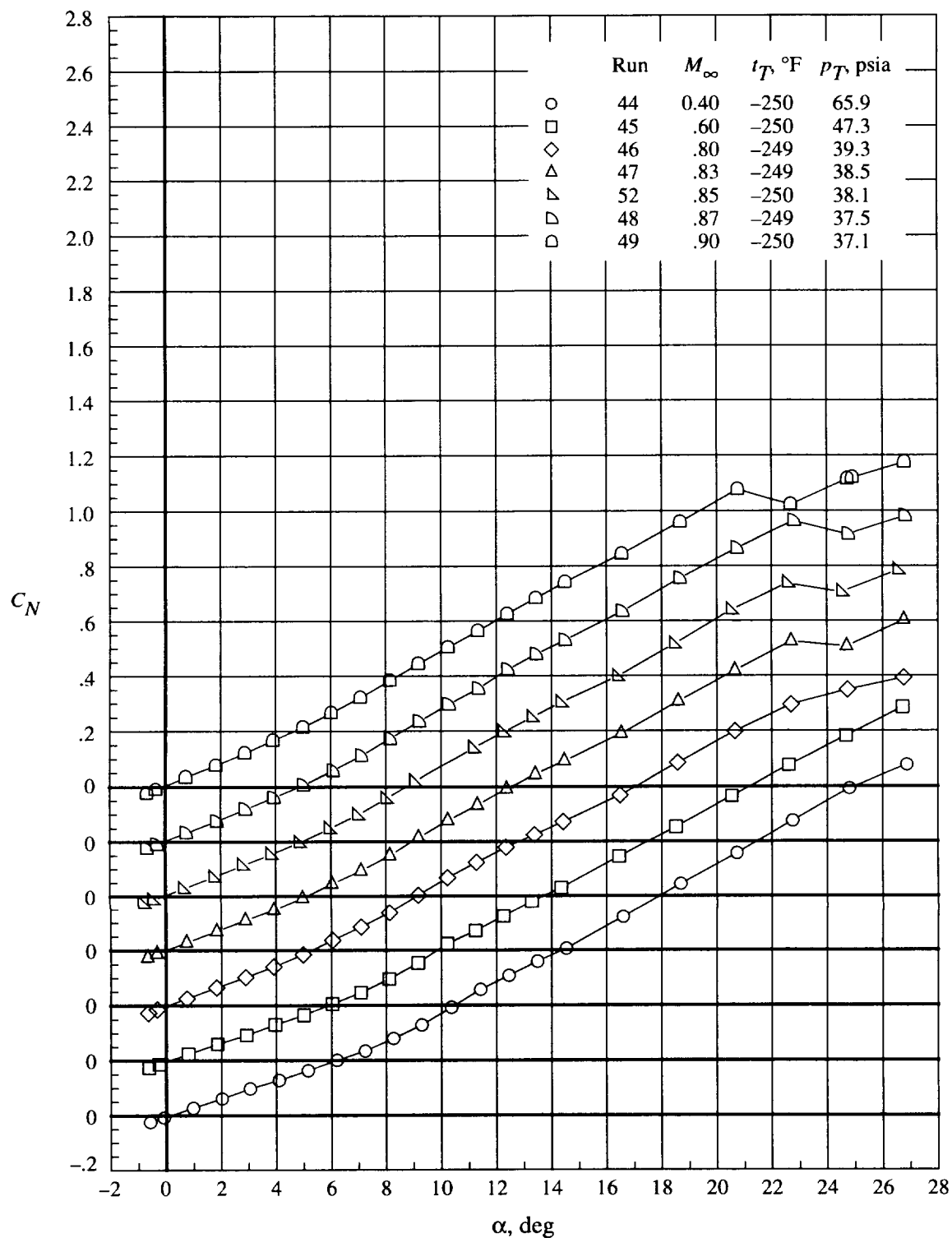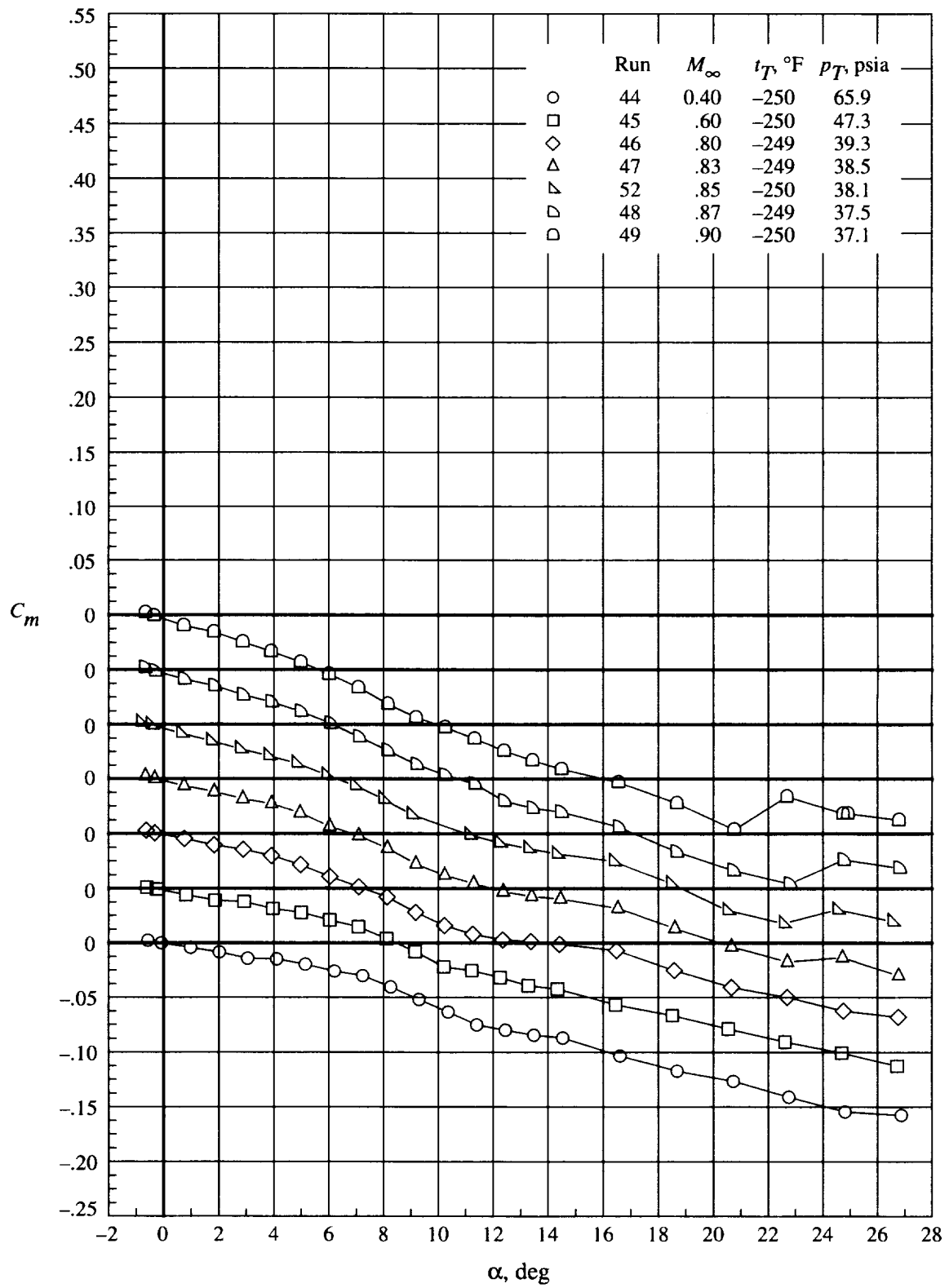(b) C_m versus α.

Figure 8. Concluded.

Appendix A

Delta Wing and Near-Field Sting Analytical Definition

General equations were used to define the leading-edge semithickness, the flat plate semithickness, the trailing-edge closure semithickness, and the transverse radius of the sting fairing. The equation φ defines the particular shape of interest (e.g., the leading-edge contour) and the equation ψ defines the boundary conditions (at $\xi = 1$) for φ. Details are as follows:

$$\xi = (x - x_0)/x_1 \qquad \text{(A1)}$$

$$\varphi(\xi) = \pm x_1\left(a\sqrt{\xi} + b\xi + c\xi^2 + d\xi^3\right) \qquad (0 \le \xi \le 1) \quad \text{(A2)}$$

$$\psi(\xi) = \pm x_1\left[\frac{l}{x_1} + m(\xi - 1) + \frac{nx_1}{2}(\xi - 1)^2\right] \qquad (1 \le \xi) \quad \text{(A3)}$$

The second-blending function ψ is defined such that

$$\psi\big|_{\xi=1} = l \qquad \frac{d\psi}{dx}\bigg|_{\xi=1} = m \qquad \frac{d^2\psi}{dx^2}\bigg|_{\xi=1} = n$$

The two functions φ and ψ are illustrated in figure A1 for the leading-edge semithickness case where $x_0 = x_{le}$.

The general analytical expressions for the coefficients in equation (A2) follow:

$$a = \sqrt{\frac{2r}{x_1}}$$

$$b = -\frac{15}{8}a + 3\frac{l}{x_1} - 2m + \frac{nx_1}{2}$$

$$c = \frac{5}{4}a - 3\frac{l}{x_1} + 3m - nx_1$$

$$d = -\frac{3}{8}a + \frac{l}{x_1} - m + \frac{nx_1}{2}$$

With these expressions

$$\varphi(1) = \psi(1) \qquad \varphi'(1) = \psi'(1) \qquad \varphi''(1) = \psi''(1)$$

and the leading-edge radius at $\xi = 0$ is r. Curvature is also continuous at $\xi = 1$.

For the delta wing model of this study, the flat plate part represented by ψ results in both m and n being zero. The reduced coefficients are

$$a = \sqrt{\frac{2r}{x_1}}$$

$$b = -\frac{15}{8}a + 3\frac{l}{x_1}$$

$$c = \frac{5}{4}a - 3\frac{l}{x_1}$$

$$d = -\frac{3}{8}a + \frac{l}{x_1}$$

For a sharp leading edge, the radius $r = 0$ and the coefficients further reduce to

$$a = 0$$

$$b = 3\frac{l}{x_1}$$

$$c = -3\frac{l}{x_1}$$

$$d = \frac{l}{x_1}$$

Specific numerical values follow for the delta wing in subsequent discussions.

Leading Edges

The streamwise leading-edge contours are designed to give leading-edge radii of 0, 0.05, 0.15, and 0.30 percent of the mean aerodynamic chord and to match the flat plate wing at a streamwise distance of 15 percent of the root chord aft of the leading edge with continuity through the second derivative. The longitudinal coordinate of the leading edge is x_{le} and the leading-edge contour is described by equation (A2), the coefficients in table A1, and the following definitions:

$$x_0 = x_{le}$$

$$x_1 = 0.15$$

Flat Plate

The flat plate center part of the wing has a uniform thickness. The equation for the semithickness is as follows:

$$x_0 = x_{le} + 0.15$$

$$x_1 = 0.9 - x_0$$

$$\varphi(\xi) = \pm 0.0170008 \qquad (0 \le \xi \le 1)$$

21

Trailing-Edge Closure Region

The streamwise trailing-edge closure is designed to produce a sharp trailing edge and to match the flat plate wing at the 90-percent root chord station with continuity through the second derivative. The closure is described by equation (A2), the coefficients in table A2, and the following definitions:

$$x_0 = 1$$
$$x_1 = 0.10$$

Sting Fairing

The sting is a body of revolution and the sting fairing is designed to emerge from the wing slightly aft of the 60-percent root chord station and to match the constant-radius part of the sting slightly ahead of the wing trailing edge. The transverse radius of the sting fairing is described by equation (A2), the coefficients in table A3, and the following definitions:

$$x_0 = 0.61057051$$
$$x_1 = 0.36916023$$

Fore-Sting

As shown in figure 3, the downstream continuation of the sting in the near field of the wing is referred to as the fore-sting. It can be subdivided into the four regions listed in table A4 for the purpose of defining the sting transverse radius φ. In region 2, the sting transverse radius increases by the radius of curvature equal to 1.979 from $x/c_R = 1.175$. (See fig. 3.) Beyond region 4, the actual sting geometry becomes more complex. For computational purposes, the sting could be either extended as is or closed out in a convenient fashion.

Table A1. Leading-Edge Coefficients for Equation (A2)

$r/\bar{c}$, percent	a	b	c	d
0	0	$3d$	$-b$	0.1133386669
.05	0.06666666666667	0.21501600073802	−0.25668266740469	.08833866691267
.15	.11547005383792	.12350964979191	−.19567843344062	.07003739672345
.30	.16329931618554	.03382978289013	−.13589185550609	.05210142334309

Table A2. Trailing-Edge Coefficients for Equation (A2)

$r/\bar{c}$, percent	a	b	c	d
0	0	$3d$	$-b$	0.17000800036901

Table A3. Sting Fairing Coefficients for Equation (A2)

$r/\bar{c}$, percent	a	b	c	d
0.27910261994295	0.10040234847327	0.33279822819157	−0.39554969598736	0.13603332984884

Table A4. Fore-Sting Transverse Radius φ

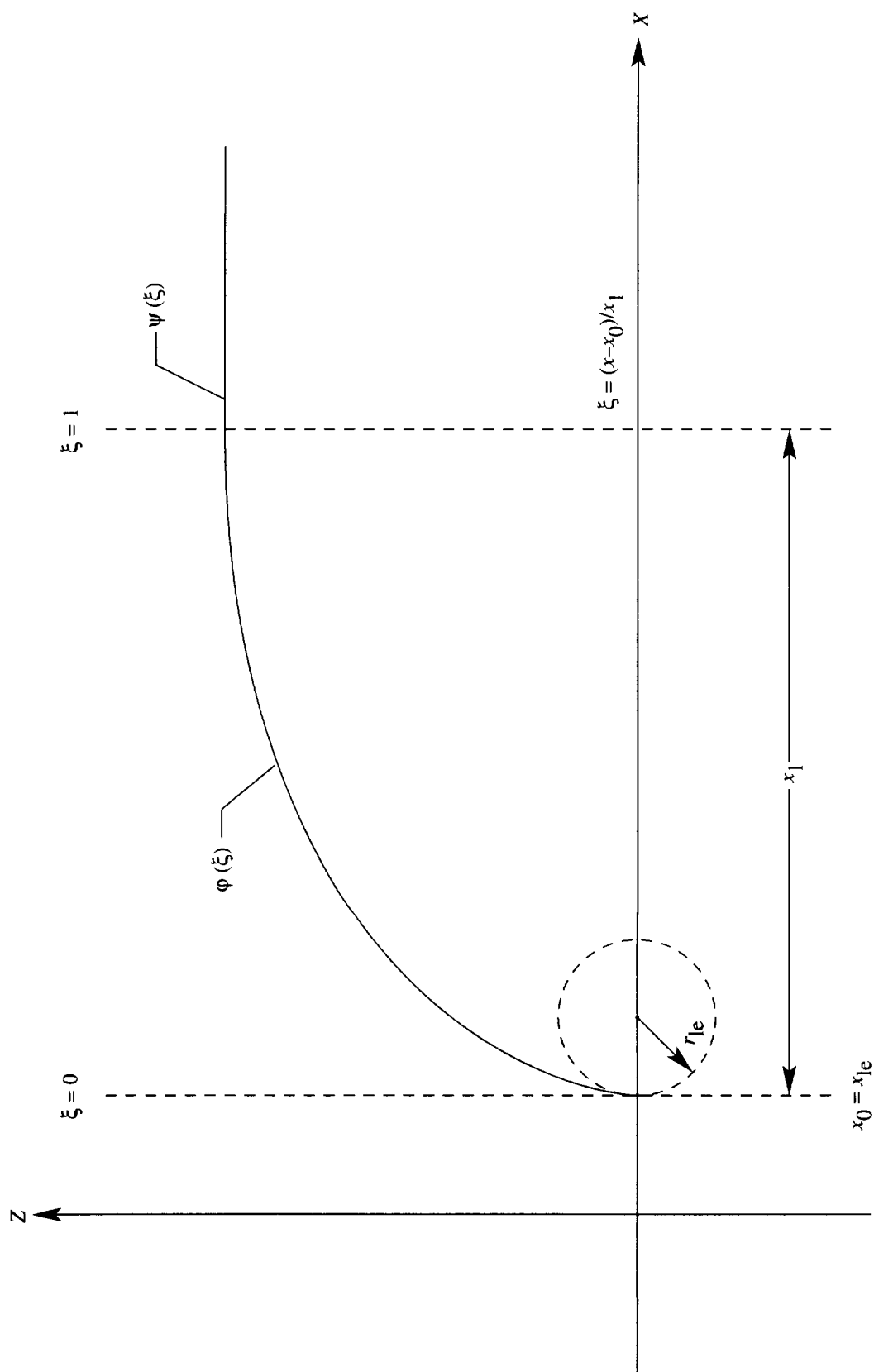| Region	Taper, deg	x/c_R		φ
1	0	From	0.9797	0.06412
		To	1.175	0.06412
2		From	1.175	0.06412
		To	1.253	0.06564
3	2.25	From	1.253	0.06564
		To	1.684	0.08258
4	0	From	1.684	0.08258
		To	1.758	0.08258

Figure A1. Delta wing semithickness functions.

Appendix B

Data Uncertainty

The uncertainties U of the measurements of the normal-force coefficient C_N, pitching-moment coefficient C_m, pressure coefficient C_p, and free-stream Mach number M_∞ depend on the uncertainties of their respective primary measurements.

The coefficients C_N, C_m, and C_p (Mach number is discussed separately) are derived by

$$C_N = \frac{F_N}{q_\infty S} \tag{B1}$$

$$C_m = \frac{M_Y}{q_\infty S \bar{c}} \tag{B2}$$

$$C_p = \frac{p - p_\infty}{q_\infty} \tag{B3}$$

The primary measurements used to define these coefficients are the normal force F_N, pitching moment M_Y, surface local static pressure p, free-stream static pressure p_∞, and free-stream total pressure p_T. The free-stream static pressure and the free-stream total pressure are used to compute the free-stream Mach number, which, in turn, is used to compute the free-stream dynamic pressure q_∞.

The free-stream dynamic pressure that accounts for the compressibility effect in high-speed flow is defined as

$$q_\infty = \frac{1}{2}\gamma p_\infty M_\infty^2 \tag{B4}$$

where γ denotes the ratio of specific heats. Substitutions for the dynamic pressure in the normal-force, pitching-moment, and pressure coefficient equations (B1), (B2), and (B3), respectively, give

$$C_N = \frac{F_N}{\frac{1}{2}\gamma p_\infty M_\infty^2 S} \tag{B5}$$

$$C_m = \frac{M_Y}{\frac{1}{2}\gamma p_\infty M_\infty^2 S \bar{c}} \tag{B6}$$

$$C_p = \frac{p - p_\infty}{\frac{1}{2}\gamma p_\infty M_\infty^2} \tag{B7}$$

The Mach number, which is not a primary measurement, is derived from the free-stream static and total pressures and the ratio of specific heats. Thus,

$$M_\infty = \left\{ \frac{2}{\gamma - 1}\left[\left(\frac{p_\infty}{p_T}\right)^{-(\gamma-1)/\gamma} - 1 \right] \right\}^{1/2} \tag{B8}$$

The coefficients are then functions of the following measured variables: the normal force, the pitching moment, the local pressure, the free-stream static pressure, and the free-stream Mach number; the Mach number is a function of the free-stream static pressure and the free-stream total pressure (i.e., stagnation pressure). The uncertainties $U(\ )$ of these primary measured variables are presented in table B1.

Table B1. Data Uncertainties

Variable	Uncertainty
$U(F_N)$, lbf	<24.0
$U(M_Y)$, in-lbf	<46.8
$U(p)$, lbf/in^2	<0.03
$U(p_T)$, lbf/in^2	<0.01
$U(p_\infty)$, lbf/in^2	<0.02

The probability of the value of each uncertainty being correct is assumed to be the same. From reference 17, the uncertainty for each of the coefficients of equations (B5)–(B8) with the same probability is

$$U(C_N) = \left\{ \left[\frac{\partial C_N}{\partial F_N} U(F_N) \right]^2 + \left[\frac{\partial C_N}{\partial p_\infty} U(p_\infty) \right]^2 \right.$$
$$\left. + \left[\frac{\partial C_N}{\partial M_\infty} U(M_\infty) \right]^2 \right\}^{1/2} \tag{B9}$$

$$U(C_m) = \left\{ \left[\frac{\partial C_m}{\partial M_Y} U(M_Y) \right]^2 + \left[\frac{\partial C_m}{\partial p_\infty} U(p_\infty) \right]^2 \right.$$
$$\left. + \left[\frac{\partial C_m}{\partial M_\infty} U(M_\infty) \right]^2 \right\}^{1/2} \tag{B10}$$

$$U(C_p) = \left\{ \left[\frac{\partial C_p}{\partial p} U(p) \right]^2 + \left[\frac{\partial C_p}{\partial p_\infty} U(p_\infty) \right]^2 \right.$$
$$\left. + \left[\frac{\partial C_p}{\partial M_\infty} U(M_\infty) \right]^2 \right\}^{1/2} \tag{B11}$$

$$U(M_\infty) = \left\{ \left[\frac{\partial M_\infty}{\partial p_\infty} U(p_\infty) \right]^2 + \left[\frac{\partial M_\infty}{\partial p_T} U(p_T) \right]^2 \right\}^{1/2} \tag{B12}$$

Equations (B5)–(B8) are used to obtain the sensitivity of the derived quantity with respect to each of the primary measurements. The uncertainty in Mach number is first determined with the nominal wind tunnel static and total pressures for representative Reynolds and Mach numbers. The sensitivity factors (i.e., quantities in partial derivatives) change as the values of the primary measure-ments change based on test Reynolds and Mach numbers. The contributions of the static pressure and total pressure measurement to the calculated uncertainty in Mach number, normal-force coefficient, pitching-moment coefficient, and pressure coefficient are listed in tables B2–B5.

Table B2. Contribution of Primary Measurements to Mach Number Uncertainty

M_∞	R_{mac}	p_T, psia	t_T, °F	$\dfrac{\partial M_\infty}{\partial p_\infty} U(p_\infty)$	$\dfrac{\partial M_\infty}{\partial p_T} U(p_T)$	$U(M_\infty)$
0.40	6×10^6	66	120	−0.0004	0.0002	0.0005
.60	6	19.5	120	−.0003	.0002	.0003
.85	120	76	−250	−.0002	.0001	.0003
.90	6	15.5	120	−.0003	.0001	.0003

Table B3. Contribution of Primary Measurements to Normal-Force Coefficient Uncertainty

M_∞	R_{mac}	p_T, psia	t_T, °F	α, deg	$\dfrac{\partial C_N}{\partial F_N} U(F_N)$	$\dfrac{\partial C_N}{\partial p_\infty} U(p_\infty)$	$\dfrac{\partial C_N}{\partial M_\infty} U(M_\infty)$	$U(C_N)$
0.40	6×10^6	66.0	120	4.84	0.01187	−0.00003	0.00037	0.0119
				9.95	0.01189	−0.00008	−0.00080	0.0119
				20.17	0.01189	−0.00019	−0.00202	0.0121
0.60	6×10^6	19.5	120	4.99	0.02020	−0.00004	−0.00019	0.0202
				10.14	0.02020	−0.00009	−0.00045	0.0202
				20.26	0.02021	−0.00022	−0.00106	0.0202
0.85	120×10^6	76.0	−250	4.95	0.00323	−0.00005	−0.00012	0.0032
				10.34	0.00322	−0.00012	−0.00030	0.0032
				14.57	0.00323	−0.00017	−0.00044	0.0033
0.90	6×10^6	15.5	120	5.06	0.01501	−0.00007	−0.00015	0.0150
				10.20	0.01500	−0.00016	−0.00034	0.0150
				20.33	0.01503	−0.00034	−0.00074	0.0150

Table B4. Contribution of Primary Measurements to Pitching-Moment Coefficient Uncertainty

M_∞	R_{mac}	p_T, psia	t_T, °F	α, deg	$\dfrac{\partial C_m}{\partial M_Y} U(M_Y)$	$\dfrac{\partial C_m}{\partial p_\infty} U(p_\infty)$	$\dfrac{\partial C_m}{\partial M_\infty} U(M_\infty)$	$U(C_m)$
0.40	6×10^6	66.0	120	4.84	0.00000	0.00000	0.00005	0.0000
				9.95	0.00000	0.00001	0.00012	0.0001
				20.17	0.00000	0.00003	0.00027	0.0003
0.60	6×10^6	19.5	120	4.99	0.00000	0.00001	0.00003	0.0000
				10.14	0.00000	0.00001	0.00007	0.0001
				20.26	0.00000	0.00003	0.00014	0.0001
0.85	120×10^6	76.0	−250	4.95	0.00000	0.00001	0.00002	0.0000
				10.34	0.00000	0.00002	0.00005	0.0001
				14.57	0.00000	0.00003	0.00006	0.0001
0.90	6×10^6	15.5	120	5.06	0.00000	0.00001	0.00003	0.0000
				10.20	0.00000	0.00003	0.00007	0.0001
				20.33	0.00000	0.00007	0.00015	0.0002

Table B5. Contribution of Primary Measurements to Pressure Coefficient Uncertainty

M_∞	R_{mac}	p_T, psia	t_T, °F	α, deg	$\dfrac{\partial C_p}{\partial p} U(p)$	$\dfrac{\partial C_p}{\partial p_\infty} U(p_\infty)$	$\dfrac{\partial C_p}{\partial M_\infty} U(M_\infty)$	$U(C_p)$
0.40	6×10^6	66.0	120	4.84	0.00458	0.00001	0.01066	0.0116
				9.95	0.00459	0.00002	0.01077	0.0117
				20.17	0.00459	0.00007	0.01101	0.0119
0.60	6×10^6	19.5	120	4.99	0.00780	0.00002	0.00231	0.0081
				10.14	0.00780	0.00005	0.00238	0.0082
				20.26	0.00780	0.00010	0.00249	0.0082
0.85	120×10^6	76.0	−250	4.95	0.00125	0.00000	0.00062	0.0014
				10.34	0.00124	0.00001	0.00062	0.0014
				14.57	0.00125	0.00001	0.00063	0.0014
0.90	6×10^6	15.5	120	5.06	0.00580	0.00002	0.00064	0.0058
				10.20	0.00579	0.00006	0.00068	0.0058
				20.33	0.00580	0.00007	0.00070	0.0058

Appendix C

Experimental Surface Pressure Data for 65° Delta Wing, $M_\infty = 0.85$

The experimental surface pressure data for the 65° delta wing at constant $M_\infty = 0.85$ are summarized in tables C1–C7. Because of the extensive data contained in these tables, they have not been included in the printed copy of the paper but are available electronically from the Langley Technical Report Server (LTRS). Open the files with the following Uniform Resource Locator (URL):

ftp://techreports.larc.nasa.gov/pub/techreports/larc/96/NASA-96-tm4645vol2appC.ps.Z

Appendix D

Experimental Surface Pressure Data for 65° Delta Wing, $R_{mac} = 6 \times 10^6$

The experimental surface pressure data for the 65° delta wing at constant $R_{mac} = 6 \times 10^6$ are summarized in tables D1–D6. Because of the extensive data contained in these tables, they have not been included in the printed copy of the paper but are available electronically from the Langley Technical Report Server (LTRS). Open the files with the following Uniform Resource Locator (URL):

ftp://techreports.larc.nasa.gov/pub/techreports/larc/96/NASA-96-tm4645vol2appD.ps.Z

Appendix E

Experimental Surface Pressure Data for 65° Delta Wing, $R_{mac} = 60 \times 10^6$

The experimental surface pressure data for the 65° delta wing at constant $R_{mac} = 60 \times 10^6$ are summarized in tables E1–E6. Because of the extensive data contained in these tables, they have not been included in the printed copy of the paper but are available electronically from the Langley Technical Report Server (LTRS). Open the files with the following Uniform Resource Locator (URL):

ftp://techreports.larc.nasa.gov/pub/techreports/larc/96/NASA-96-tm4645vol2appE.ps.Z

References

1. Winter, H.: *Flow Phenomena on Plates and Airfoils of Short Span.* NACA TM-798, 1936.

2. Wilson, Herbert A.; and Lovell, J. Calvin: *Full-Scale Investigation of the Maximum Lift and Flow Characteristics of an Airplane Having Approximately Triangular Plan Form.* NACA RM L6K20, 1947.

3. Örnberg, Torsten: *A Note On the Flow Around Delta Wings.* KTH-Aero TN 38, Div. of Aeronautics, R. Inst. of Technology (Stockholm), 1954.

4. Lawford, J. A.: *Low-Speed Wind Tunnel Experiments on a Series of Sharp-Edged Delta Wings—Part II. Surface Flow Patterns and Boundary Layer Transition Measurements.* Tech. Note Aero. 2954, R. Aircr. Establ., Mar. 1964.

5. Hummel, Ing. Dietrich: On the Vortex Formation Over a Slender Wing at Large Angles of Incidence. *High Angle of Attack Aerodynamics*, AGARD-CP-247, Jan. 1979, pp. 15-1–15-17.

6. Vorropoulos, G.; and Wendt, J. F.: Laser Velocimetry Study of Compressibility Effects on the Flow Field of a Delta Wing. *Aerodynamics of Vortical Type Flows in Three Dimensions*, AGARD-CP-342, July 1983, pp. 9-1–9-13. (Available from DTIC as AD A135 157.)

7. Poisson-Quinton, P.: Slender Wings for Civil and Military Aircraft. *Israel J. Technol.*, vol. 16, no. 3, 1978, pp. 97–131.

8. Skow, A. M.; and Erickson, G. E.: Modern Fighter Aircraft Design for High-Angle-of-Attack Maneuvering. *High Angle-of-Attack Aerodynamics*, AGARD-LS-121, Dec. 1982, pp. 4-1–4-59.

9. Polhamus, E. C.: Applying Slender Wing Benefits to Military Aircraft. *J. Aircr.*, vol. 21, no. 8, Aug. 1984, pp. 545–559.

10. Polhamus, E. C.; and Gloss, B. B.: Configuration Aerodynamics. *High Reynolds Number Research*, NASA CP-2183, 1980, pp. 217–234.

11. Henderson, William P.: *Effects of Wing Leading-Edge Radius and Reynolds Number on Longitudinal Aerodynamic Characteristics of Highly Swept Wing-Body Configurations at Subsonic Speeds.* NASA TN D-8361, 1976.

12. Howe, J. T.: *Some Fluid Mechanical Problems Related to Subsonic and Supersonic Aircraft.* NASA SP-183, 1969.

13. Henderson, William P.: *Studies of Various Factors Affecting Drag Due to Lift at Subsonic Speeds.* NASA TN D-3584, 1966.

14. Fuller, Dennis E.: *Guide for Users of the National Transonic Facility.* NASA TM-83124, 1981.

15. Plentovich, E. B.: *The Application to Airfoils of a Technique for Reducing Orifice-Induced Pressure Error at High Reynolds Numbers.* NASA TP-2537, 1986.

16. Hall, Robert M.; and Adcock, Jerry B.: *Simulation of Ideal-Gas Flow by Nitrogen and Other Selected Gases at Cryogenic Temperatures.* NASA TP-1901, 1981.

17. Holman, Jack Philip: *Experimental Methods for Engineers.* 4th ed., McGraw-Hill Book Co., 1984, pp. 46–99.

18. Foster, Jean M.; and Adcock, Jerry B.: *User's Guide for the National Transonic Facility Data System.* NASA TM-100511, 1987.

REPORT DOCUMENTATION PAGE

Public reporting burden for this collection of information is estimated to average 1 hour per response, including the time for reviewing instructions, searching existing data sources, gathering and maintaining the data needed, and completing and reviewing the collection of information. Send comments regarding this burden estimate or any other aspect of this collection of information, including suggestions for reducing this burden, to Washington Headquarters Services, Directorate for Information Operations and Reports, 1215 Jefferson Davis Highway, Suite 1204, Arlington, VA 22202-4302, and to the Office of Management and Budget, Paperwork Reduction Project (0704-0188), Washington, DC 20503.

1. AGENCY USE ONLY *(Leave blank)*	2. REPORT DATE February 1996	3. REPORT TYPE AND DATES COVERED Technical Memorandum

4. TITLE AND SUBTITLE
Experimental Surface Pressure Data Obtained on 65° Delta Wing Across Reynolds Number and Mach Number Ranges
Volume 2—Small-Radius Leading Edge

5. FUNDING NUMBERS
WU 505-59-54-01

6. AUTHOR(S)
Julio Chu and James M. Luckring

7. PERFORMING ORGANIZATION NAME(S) AND ADDRESS(ES)
NASA Langley Research Center
Hampton, VA 23681-0001

8. PERFORMING ORGANIZATION REPORT NUMBER
L-17411B

9. SPONSORING/MONITORING AGENCY NAME(S) AND ADDRESS(ES)
National Aeronautics and Space Administration
Washington, DC 20546-0001

10. SPONSORING/MONITORING AGENCY REPORT NUMBER
NASA TM-4645, Vol. 2

11. SUPPLEMENTARY NOTES

12a. DISTRIBUTION/AVAILABILITY STATEMENT
Unclassified–Unlimited
Subject Category 02
Availability: NASA CASI (301) 621-0390

12b. DISTRIBUTION CODE

13. ABSTRACT *(Maximum 200 words)*

An experimental wind tunnel test of a 65° delta wing model with interchangeable leading edges was conducted in the Langley National Transonic Facility (NTF). The objective was to investigate the effects of Reynolds and Mach numbers on slender-wing leading-edge vortex flows with four values of wing leading-edge bluntness. Experimentally obtained pressure data are presented without analysis in tabulated and graphical formats across a Reynolds number range of 6×10^6 to 84×10^6 at a Mach number of 0.85 and across a Mach number range of 0.4 to 0.9 at Reynolds numbers of 6×10^6 and 60×10^6. Normal-force and pitching-moment coefficient plots for these Reynolds number and Mach number ranges are also presented.

14. SUBJECT TERMS
Aerodynamics; Delta wing; Reynolds number; Leading-edge bluntness; Vortex flow; Cryogenic testing

15. NUMBER OF PAGES
31

16. PRICE CODE
A03

17. SECURITY CLASSIFICATION OF REPORT Unclassified	18. SECURITY CLASSIFICATION OF THIS PAGE Unclassified	19. SECURITY CLASSIFICATION OF ABSTRACT Unclassified	20. LIMITATION OF ABSTRACT